Research Article | Vol. 27, No. 26 / 23 December 2019 / Optics Express 38698

Optics EXPRESS

Silicon ring resonators with a free spectral range robust to fabrication variations

BOLING OUYANG,[1,*] YUFEI XING,[2,3] WIM BOGAERTS,[2,3] AND JACOB CARO[1]

[1] *Department of Imaging Physics, Delft University of Technology, Lorentzweg 1, 2628 CJ Delft, The Netherlands*
[2] *Photonics Research Group, Ghent University-imec, Technologiepark-Zwijnaarde 126, 9052 Ghent, Belgium*
[3] *Center for Nano-and Biophotonics, Ghent University, Technologiepark-Zwijnaarde 126, 9052 Ghent, Belgium*
[*] *b.ouyang@tudelft.nl*

Abstract: We propose a design method for silicon ring resonators (RRs) with a free spectral range (FSR) insensitive to fabrication variations. Two waveguide-core widths are used in the RR, with opposite signs of the group-index derivative with respect to the width. This results in cancellation of the width-dependent FSR changes. The systematic deviation of the realized width from the design width is determined and is used for calibrating the calculated relation of group index versus width. This enables a more accurate FSR value and well-aimed robust performance. We present two robust design examples. Experimental results match well with the predictions. For the deliberately introduced ±10 nm core-width change, the FSR variation of the robust designs is only about 30% of the value measured from the RR with a single core width. This design method can be used to improve the performance of photonic integrated circuits using multiple RRs. As the FSR of a RR is not easily tunable, the robust design is beneficial to applications where an accurate FSR is required, such as in microwave photonics.

1. Introduction

Silicon photonics has become a highly promising platform for photonic integrated circuits (PICs). Benefiting from a high refractive index contrast and a CMOS compatible fabrication process, silicon photonics enables a small device footprint, high-density packing, large-scale integration, and high-volume, low-cost production. However, the strong light confinement of silicon photonics and the nanometer-scale dimensions of the photonic structures also lead to high sensitivity of device properties to waveguide-width variations inherent to the fabrication process [1]. As a result, the performance of the PIC will deviate from the designed one. With the upscaling of PICs, the performance deviations can accumulate and get more severe rapidly, ruining the functionality. The width variations of the waveguide core result from inherent variations of various steps in the fabrication process, e.g., lithography dose and etch rate, making these variations unavoidable. Even for a well-developed silicon photonics foundry, the fabricated core width can have tens of nanometers systematic deviation from the design value, with notable variations across the wafer superimposed on the systematic deviations [2–4]. Therefore, robust optimization methods for minimizing the effects of variability in the phase of the PIC design are crucial for further developing silicon photonics [5].

Mach-Zehnder interferometers (MZIs) and ring resonators (RRs) are commonly used silicon photonic devices. Fabrication tolerant design of silicon MZIs with a robust peak-wavelength positioning has already been reported [6]. By utilizing different widths for the two arms of the

#381643 https://doi.org/10.1364/OE.381643
Journal © 2019 Received 30 Oct 2019; revised 5 Dec 2019; accepted 6 Dec 2019; published 20 Dec 2019

Optics EXPRESS

MZI, width-variation induced effective index changes can be compensated, enabling a wavelength shift of < 60 pm per nm width variation [6]. Similar approaches have been used for making thermally robust MZIs [7–10], again taking advantage of the two optical paths.

Unlike MZIs, RRs have only a single optical path. So, the method used for MZIs cannot be used to make the RR resonance wavelength insensitive to fabrication variations. Therefore, the resonance wavelength is, in practice, often tuned thermally after fabrication [11]. Another important RR quantity is the free spectral range (FSR), which is influenced by waveguide-width variations as well. Accurate control of the FSR is needed in many applications. For example, the channel spacing of wavelength filters and wavelength division multiplexers [12–15] based on RRs relies on the FSR. The channel spacing of such devices can go down to 25 GHz in telecom applications in the C-band, where high channel-spacing accuracy is needed. In microwave photonic applications, the FSR of the RR can be used to select carrier frequencies [16], requiring large rings with an accurate FSR. Further, the RR is a basic component of programmable PICs [17]. When these programmable PICs become large, it is important to have control of the FSR of RRs across the entire chip. The thermal tunability of the FSR is rather limited. Therefore, there is a clear need for a design method that yields a robust, well-controlled FSR for silicon RRs.

Here, we propose and demonstrate a design method for silicon RRs with an FSR robust to fabrication variations. The method is based on using two waveguide widths in the RR with opposite signs of $\partial n_g/\partial w$ (n_g = group index, w = core width), resulting in cancellation of the effect of fabrication-induced width variations on the FSR. For the design of robust RRs according to our method, we derive a design rule and calibrate the design inputs using our experimental determination of the systematic width deviation. We successfully test the design method, both numerically and experimentally, by comparison with results from RRs designed in the normal way, i.e., with a single waveguide width. This method does not require adjustment of the fabrication process. Our method is another example of a generic design approach that exploits cancellation effects used in MZIs [6–10]. To our knowledge, this is the first time that in a RR cancellation effects using two waveguides are exploited.

2. Design method

2.1. Ring-resonator design with a robust free spectral range

The FSR of a RR with a single waveguide width, expressed as frequency difference, is given by

$$\mathrm{FSR}_f = \frac{c}{n_g L}. \tag{1}$$

Here, c is the speed of light in vacuum. L is the circumference of the RR. Within a first order approximation of the dispersion and expressed as a wavelength difference, the FSR equals

$$\mathrm{FSR}_\lambda = \frac{\lambda^2}{n_g L}, \tag{2}$$

where λ is the operation wavelength. As c is a constant and λ is virtually constant, while L in general has a very small deviation from the design value, fabrication-induced FSR variations dominantly originate from n_g variations.

To obtain the waveguide-width dependence of n_g for the guided transverse electric TE_0 mode in our waveguide, the basis of our design method, we use finite element simulations with COMSOL. We sweep the width of air-cladding silicon strip waveguides from 305 nm to 520 nm, using a 220 nm height and an 85° sidewall angle of the waveguide (angle given by the IMEC technology handbook; all devices used in this work have been fabricated at IMEC through the Europractice MPW service). In Fig. 1 we present the calculated n_g as a function of waveguide width w at λ = 1550 nm, with in the inset the calculated TE_0 mode profile of the waveguide with

Optics EXPRESS

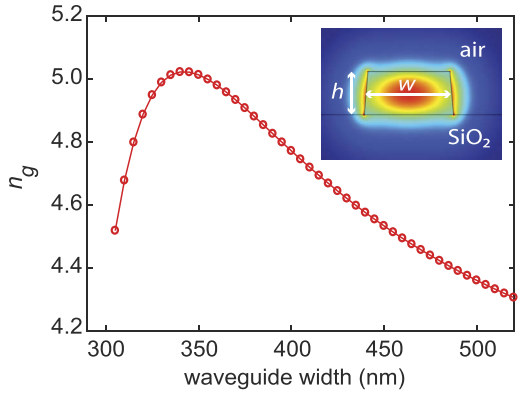

Fig. 1. Calculated group index n_g of air-cladding silicon waveguides (h = 220 nm) as a function of waveguide width w at λ = 1550 nm. As an example, the inset shows the profile of the TE_0 mode with w = 450 nm and h = 220 nm, for which n_g is calculated.

w = 450 nm. $n_g(w)$ is a relatively strong function in this width range, showing a relative change of up to 17%. n_g reaches a maximum for w = 340 nm. Thus, the derivative $\partial n_g/\partial w$ reverses sign when crossing w = 340 nm. Our design method is based on this sign reversal.

Using two widths $w1$ and $w2$ for the RR, the FSR can be expressed as

$$\mathrm{FSR}_f = \frac{c}{n_g(w1)L_{w1} + n_g(w2)L_{w2} + 2\overline{n_{g,t}}L_t}\,. \tag{3}$$

Here, L_{w1} and L_{w2} are the two waveguide lengths. L_t is the length of the taper. $n_g(w1)$ and $n_g(w2)$ are the corresponding group indices. $\overline{n_{g,t}}$ is the average group index of the tapers. Figure 2 shows the schematic of this RR design robust to width variations. The condition for this robustness is expressed by the following design rule:

$$\left.\frac{\partial n_g(w)}{\partial w}\right|_{w1} L_{w1} + \left.\frac{\partial n_g(w)}{\partial w}\right|_{w2} L_{w2} = 0\,. \tag{4}$$

Equation (4) can be satisfied for opposite signs of the derivatives, i.e., for $w1$ and $w2$ on each side of the maximum of $n_g(w)$. Thus, the effect of fabrication-induced n_g variations on the FSR can be cancelled for proper choice of L_{w1} and L_{w2}. In this, we assume that the variations of $w1$ and $w2$ have a very similar and small magnitude, such that both derivatives may be considered as

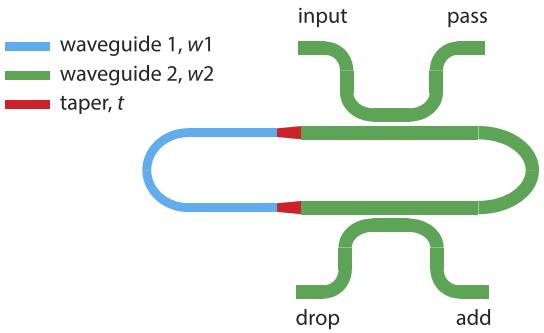

Fig. 2. Schematic of the RR design with two waveguide widths, giving an FSR robust to waveguide-width variations.

Optics EXPRESS

constant. The effect of tapers is neglected in Eq. (4), because these are very short compared to the circumference of the RR. Besides, the abovementioned cancellation effect also occurs between the wide and narrow side of a taper.

2.2. Calibration of the design inputs using the systematic width deviation

As can be seen in Fig. 1, the width-dependence of $\partial n_g/\partial w$ is particularly strong below 340 nm, making it hard to satisfy Eq. (4) for fabricated widths with a strong systematic deviation from the design value. This implies that the systematic deviation of the widths needs to be known. The systematic width deviation for the IMEC process is provided for a rather limited number of design values as part of their design kit. Therefore, we experimentally determine the systematic width deviation from measurements of the optical transmission of ten test MZIs. These MZIs have a constant path-length difference ΔL, but various waveguide widths. The width of the two arms of the MZIs is the same, ranging from 310 nm to 490 nm among the MZIs. The applied wavelength range is 1549 – 1551 nm. A cosine function, the common transmission function of an MZI, is fitted to the measured transmission curves, yielding the FSR of each MZI as a fit parameter. The FSR, in turn, gives the n_g of the waveguide at $\lambda = 1550$ nm, using the equivalent of Eq. (2), with L replaced by ΔL. Figure 3(a) shows an example of a measured MZI transmission spectrum, for a design width of 450 nm, along with the cosine fitted to the data points.

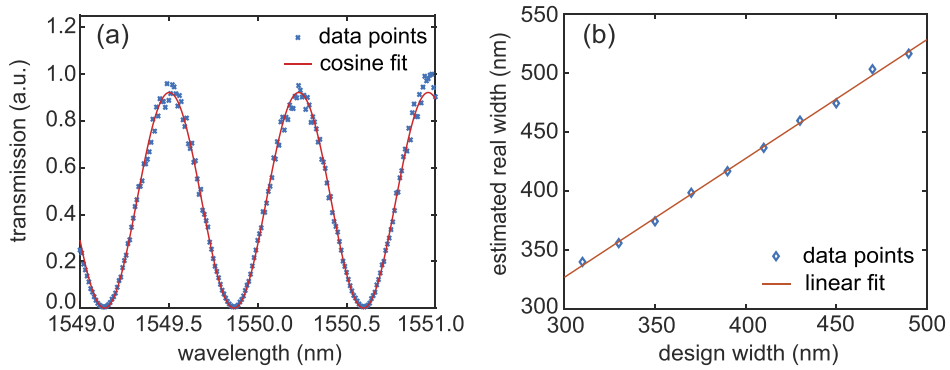

Fig. 3. (a) Measured transmission of a test MZI with a design width of 450 nm, together with the fitted cosine. (b) Estimated real waveguide width as a function of design width.

To arrive at a single n_g value for each width that sufficiently represents the whole wafer, we measure several MZIs of the same design across a proper fraction of the wafer and repeat the n_g extraction. The final experimental n_g values for each width are obtained by averaging over the extracted values from MZIs of the same design. In this procedure, the n_g variations across the wafer are averaged out to a certain extent.

For each design width, we then estimate the real width after fabrication with the aid of the simulated n_g versus w relation in Fig. 1, which we use as a lookup table. By picking the various measured n_g values in the simulation data, we find the fabricated width of the measured MZIs. Here, we use as a guide that according to the IMEC technology handbook the fabricated width exceeds the design width. Moreover, this width bias should depend smoothly on the design width. As we are using average n_g values, our procedure gives the best estimate of the average real width, while across the wafer the width will vary around the estimate. This procedure leads to the relation between the design width and the estimated real width presented in Fig. 3(b), which also shows a high quality linear fit to the data points. The relation provides the systematic width deviation for designs in this work. From our estimate, the fabricated width for the design width of 450 nm is 478.1 nm. This is rather close to 475.4 nm stated in the IMEC handbook.

Optics EXPRESS

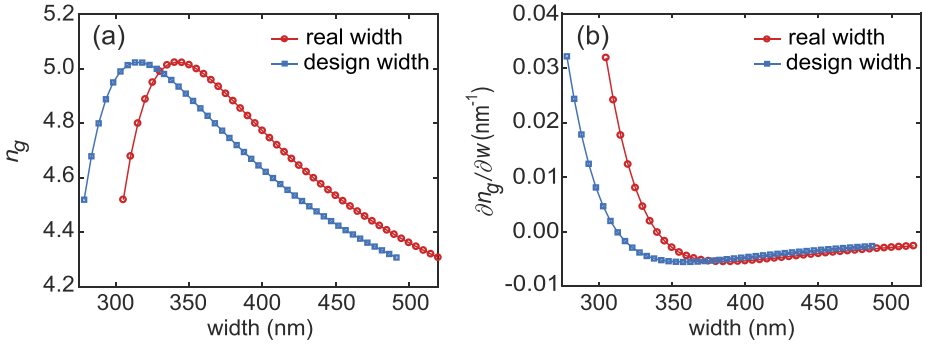

Fig. 4. (a) n_g versus width. The blue curve is obtained by calibrating the red curve from Fig. 1 using the linear function in Fig. 3(b). (b) Derivative curves $\partial n_g/\partial w$ calculated from the curves in (a).

Using the linear fit in Fig. 3(b), the function $n_g(w)$ in Fig. 1 can now be calibrated to take into account the width-dependent core-width increase after fabrication. Assuming the width in Fig. 1 is the real width, the corresponding design width is calculated using the linear function in Fig. 3(b). This process yields the calibrated function (blue curve) in Fig. 4(a), which has shifted to the left with respect to the red curve. Plots of the related derivative curves $\partial n_g/\partial w$ are shown in Fig. 4(b). The calibrated n_g and $\partial n_g/\partial w$ curves serve as inputs for Eqs. (3) and (4) in the design process of robust RRs.

3. Design implementation

Here, we study in detail two designs for robust RRs, robust 1 and robust 2. We choose FSR = 1 nm (124.783 GHz) at $\lambda = 1550$ nm. Robust 1 has design widths $w1 = 296$ nm and $w2 = 450$ nm. $w2$ is a commonly used width, which has a negative $\partial n_g/\partial w$ value. The value of $w1$ is chosen such that the derivative $\partial n_g/\partial w$ is positive, but relatively small. This is to arrange, according to the shape of $\partial n_g/\partial w$ in Fig. 4(b), that $\partial n_g/\partial w$ varies relatively weakly for width variations around $w1$. In this way, the range of width variations that can be tolerated before the design rule [Eq. (4)] breaks down is maximized. Using the same argument, we arrive for robust 2 at the values $w1 = 300$ nm and $w2 = 360$ nm. For both robust RRs the taper length is 9 µm, enabling a smooth transition between the two widths. The average group index $\overline{n_{g,t}}$ of the tapers is calculated by averaging the group indices of the waveguides with the widths between $w1$ and $w2$, using the points of the calibrated curve in Fig. 4(a). For robust 1 and robust 2, this gives average group index values of 4.76 and 4.96, respectively. The values of L_{w1} and L_{w2} are calculated using Eqs. (3) and (4). For robust 1 (robust 2), we obtain $L_{w1} = 120.4$ µm (212.1 µm) and $L_{w2} = 389.5$ µm (260.2 µm).

To demonstrate the robustness of the FSR of robust 1 and robust 2 to width variations, we duplicate these devices by applying intentional width variations of ±6 nm, ±10 nm and ±20 nm, and calculate the predictions for the FSR using Eq. (3) and the calibrated n_g curve. Thus, design sets result that each have seven devices. For comparison, we also include a RR with a single design width of 450 nm and implement the same width variations. For this normal design, we use the red curve in Fig. 4(a), as would be done without prior knowledge of the systematic width increment. Similar to the robust RRs, the geometry of the normal design RRs is a racetrack. The total length of the normal design RRs is 529.8 µm. All RRs have the same bend radius of 30 µm. The directional coupler gap of all RRs is designed to be 250 nm when there is no intentional width change. The calculated results are given in Fig. 5. For the range given by the ±10 nm variation, the FSR variation for robust 1 and robust 2, defined by the maximum FSR minus

Optics EXPRESS

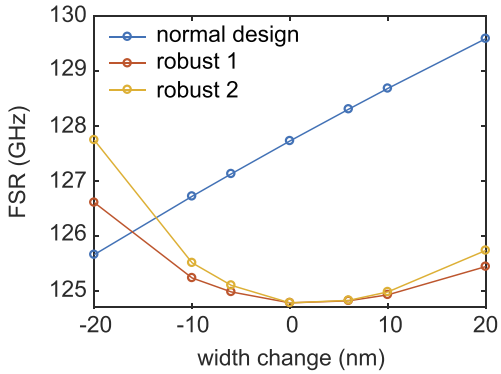

Fig. 5. Predicted FSR as a function of waveguide-width variation, for devices robust 1 and robust 2. For comparison, the behavior for a normal design is also included.

the minimum FSR in the range, is only 23% and 37% of the normal design's FSR variation, respectively. This clearly indicates that the design method works in theory and thus is ready for application in RR fabrication.

4. Experiment results

To make an experimental test of our design method, robust RRs and normal design RRs have been fabricated in one MPW run, which followed the run of the test MZIs. RRs from four dies are characterized, for comparison of the FSR values. The die locations cover the range from the center to the edge of the 200 mm wafer. The pitch of the dies is 21.84 mm. Transmission spectra of the RRs are measured by sweeping the wavelength of a tunable laser coupled to the input port of the RR and measuring the output power at the pass port with a photodetector. The transmission spectrum of RR robust 1 on die 3 is presented in Fig. 6(a), showing ten resonance dips. The depth of the dips shows a rather strong variation (8.6 dB) across the spectrum. This results from unresolved resonance splittings due to backscattering in the ring [18], with the degree of splitting and its asymmetry depending on wavelength. We find, as expected according to this explanation, that variation of the dip depth occurs in a similar way for the normal design RRs. This indicates that indeed the observed behavior is not due to the robust design. Attribution of the behavior to resonance splitting is confirmed from the somewhat deviating line shape of the dips of smaller depth. For example, the dip close to 1551.2 nm [marked with an arrow in Fig. 6(a)] shows a rather small, but observable asymmetry, contrary to the deeper dips, and has a full width at half minimum exceeding that of the deeper dips, features typical for a (weak) asymmetric resonance splitting.

From the spectrum, the FSR at 1550 nm is extracted as follows. We first normalize the spectrum and locate the two resonance dips near 1548 and 1552 nm, each in a 1 nm wavelength range. We then fit the following function for the transmission at the pass port of an add-drop RR [19] to the dips:

$$T_{\mathrm{pass}}(\lambda) = a\frac{(\lambda-\lambda_r)^2+\varepsilon\,(\gamma_r/2)^2}{(\lambda-\lambda_r)^2+(\gamma_r/2)^2}\,. \tag{5}$$

λ_r and γ_r are the resonance wavelength and the full width at half minimum of the dip, respectively. ε gives the transmission level at λ_r. The prefactor a is included, as the wing of the dip may not reach the value unity due to the overall spectrum normalization. The measured dip near 1552 nm in Fig. 6(a) is shown in Fig. 6(b), together with the resulting fit. For the two dips, the fits yield the two λ_r values, which span 4 FSRs. The curve fitting also yields the confidence bounds of the λ_r values. We use these to obtain the uncertainty of the FSR to be calculated. In spite of the

Optics EXPRESS

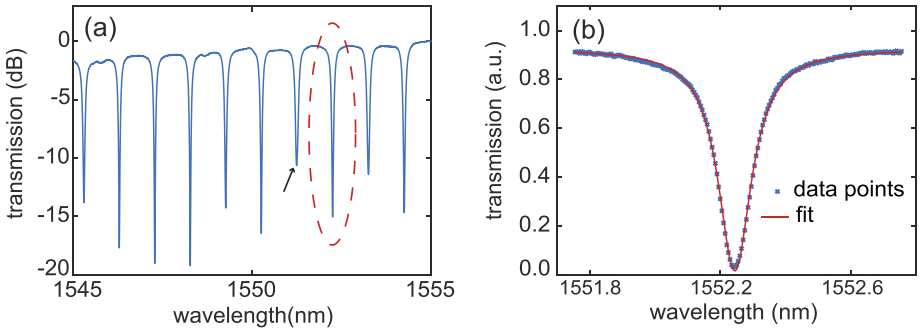

Fig. 6. (a) Measured normalized transmission spectrum of RR robust 1 from die 3. (b) Zoom-in of the dip near 1552 nm in (a) (highlighted by the red ellipse). The red curve is a fit of Eq. (5) to the data points.

weak resonance splitting, the quality of the fit of Eq. (5) to the measured dips is high. The weak asymmetry of the dip may slightly influence the quality of fits. But this influence is taken care of by the confidence bounds of the fits and is reflected in the error bars of the FSR points, which are small, as can be seen in Fig. 7. By converting the λ_r values to frequencies in vacuum and dividing the frequency difference by 4, we arrive at the FSR at 1550 nm expressed as a frequency difference. In this procedure, which we follow for all measured FSRs discussed below, we neglect the dispersion of the FSR, since the range considered is short.

Figure 7(a) shows the measured FSRs of the RRs robust 1 and robust 2 and of the normal design RR, from the four dies with locations as given in the inset of the figure. These RRs do not have intentional width variations. For robust 1 and robust 2, the FSR first decreases very similarly from die 1 to die 3 and then shows a somewhat dissimilar increase from die 3 to die 4. Along with this, the FSR of the normal design decreases from die 1 to die 4, i.e., from the wafer center towards its edge. The latter behavior is explained from a width decrease between die 1 and die 4 [see Eq. (1) and Fig. 4(a)]. Such a width decrease towards the wafer edge agrees with the results in [3,4]. This decrease for the normal design also applies to robust 1 and robust 2, leading to a minimum of FSR on die 3. The FSR behavior of these robust RRs is consistent with the FSR behavior in Fig. 5, which shows a minimum with decreasing width as well. The minimum suggests that the robust RRs of die 3 obey $\partial \mathrm{FSR}/\partial \mathrm{w} \approx 0$, implying that the realized width on die 3 is closest to the estimate of Fig. 3(b). It is logical that a die between the wafer

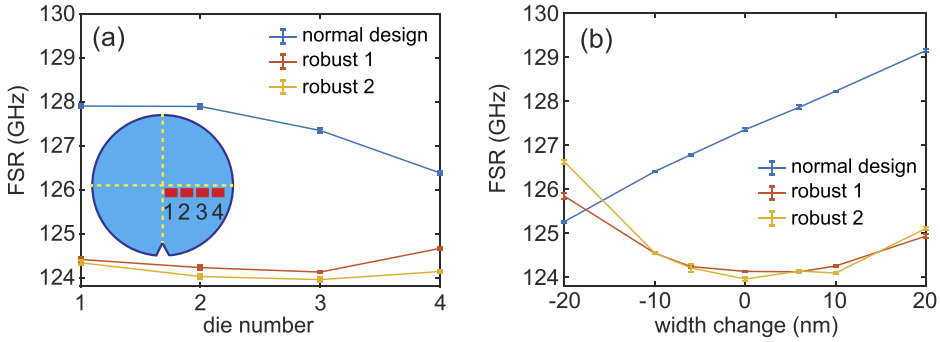

Fig. 7. (a) Measured FSRs from die 1 to die 4, for RRs without intentional width variations. The inset shows the die locations on the wafer. (b) The measured FSR from die 3 as a function of intentional waveguide-width change.

Optics EXPRESS

center and edge, in this case die 3, gives results closest to our estimate, since the width decreases from the center to the edge and the relation in Fig. 3(b) (used to obtain the design inputs for the robust RRs) represents the average width deviation across the wafer. Further, the FSR of the robust RRs is considerably closer to the design value (124.783 GHz) than the FSR of the normal design. This goes together with a clearly smaller FSR variation across the dies for the robust RRs than for the normal design RR. The findings from Fig. 7(a) constitute experimental proof for the validity of our design method for robust devices.

Because the widths on die 3 are closest to the estimate, we further measure the RRs with deliberately applied width variations on die 3. This leads to the FSR values in Fig. 7(b). The FSR behavior of robust 1, robust 2 and the normal design is highly similar to that in Fig. 5, albeit that the FSR values from die 3 are slightly smaller. This provides further proof that our method works. The FSR difference may result from the interplay of several possible causes not considered here, such as a small variation of the waveguide height and a small change for this fabrication run of the function describing the systematic width deviation [given in Fig. 3(b)]. We also see the strong similarity of Fig. 5 and Fig. 7(b) as an apparent proof that reliable determination of the FSR is indeed not prevented by occurrence of the unresolved splittings of transmission dips discussed above.

In Table 1 we give the deviation of the FSR from the design value and the range-dependent FSR variation, Δ_{FSR}. For example, for the [−10 nm, 10 nm] range, Δ_{FSR} of robust 1 and robust 2 are only 23% and 32% of Δ_{FSR} measured from the normal design, respectively. These more detailed results from die 3 confirm the validity of our method. Though the FSR variation of robust RRs becomes larger for deliberately applied width changes approaching −20 nm due to breakdown of the design rule [see Eq. (4)], this will rarely occur in practice. For a well-developed foundry such as ours (IMEC), the width change across a 200 mm wafer is mostly within 20 nm [3,4]. By using the calibration of the systematic width deviation of Fig. 3(b), the fabrication-induced width changes across the wafer will thus mainly occur in the [−10 nm, 10 nm] range (total change still 20 nm) around the estimated real width. Therefore, for the robust RRs, the resulting FSR variations will have small magnitudes according to the values we obtain in Table 1 for the [−10 nm, 10 nm] range by applying intentional width variations. FSR variations with stronger magnitudes due to fabrication-induced width variations are not likely to occur. This is proven in Fig. 7(a), where the data points only involve fabrication-induced effects on the FSR.

Table 1. Measured FSR deviations from the design value (124.783 GHz) and range-dependent FSR variations Δ_{FSR} for the measured devices on die 3. The uncertainty of each number results from the uncertainties of the FSR values derived from the transmission data. The uncertainties of the FSR values result from the confidence bounds of the two λ_r values (see Section 4), using uncertainty propagation.

	normal design (w = 450 nm)	robust 1 ($w1$ = 296 nm) ($w2$ = 450 nm)	robust 2 ($w1$ = 300 nm) ($w2$ = 360 nm)
FSR deviation (GHz)	2.56 ± 0.04	0.66 ± 0.02	0.83 ± 0.05
Δ_{FSR} (GHz), [−6 nm, 6 nm] range	1.08 ± 0.05	0.12 ± 0.04	0.3 ± 0.1
Δ_{FSR} (GHz), [−10 nm, 10 nm] range	1.82 ± 0.03	0.42 ± 0.04	0.59 ± 0.06
Δ_{FSR} (GHz), [−20 nm, 20 nm] range	3.89 ± 0.04	1.72 ± 0.08	2.66 ± 0.07

5. Conclusion and outlook

In conclusion, we have demonstrated an approach for making the FSR of silicon RRs robust to waveguide-width variations, comprising two steps: i) Estimating the systematic width deviation using transmission measurements on test MZIs, leading to calibration of our calculated $n_g(w)$

Optics EXPRESS

and $\partial n_g/\partial w(w)$ functions and ii) Including two waveguide widths in a single RR. The two widths have opposite signs of $\partial n_g/\partial w$, thus compensating the FSR variation resulting from width variations superimposed on the systematic deviation. For two design cases, we aim for an FSR of 124.783 GHz (1 nm). Measurements show that the FSR deviation and variation of the robust designs drop clearly compared to those of the normal design. For the deliberately introduced ±10 nm width change, the FSR variations in this range are only 0.42 GHz and 0.59 GHz for the two robust designs. These values are about 30% of the value measured from the normal design.

Our method, a new example of the generic design method that exploits cancellation effects using two waveguides, can be applied to PICs comprising multiple RRs. As a step in this direction, it will be important to explore the design freedom for the robust RRs in obtaining certain characteristic quantities (e.g., a predefined quality factor) subject to the restrictions imposed by the two waveguide widths and lengths, in particular the narrow width (≈ 300 nm in this work) in view of its higher propagation loss. In this, the loss in the directional couplers should be taken into account and tailored. Finally, our type of estimate of the systematic width deviation and the resulting calibration of the design inputs can be applied to other robust methods in [6–10] for more accurate designs, effectively improving performance.

Funding

Nederlandse Organisatie voor Wetenschappelijk Onderzoek (13534).

Disclosures

The authors declare no conflicts of interest.

References

1. W. Bogaerts, Y. Xing, and U. Khan, "Layout-aware variability analysis, yield prediction, and optimization in photonic integrated circuits," IEEE J. Sel. Top. Quantum Electron. **25**(5), 1–13 (2019).
2. Z. Lu, J. Jhoja, J. Klein, X. Wang, A. Liu, J. Flueckiger, J. Pond, and L. Chrostowski, "Performance prediction for silicon photonics integrated circuits with layout-dependent correlated manufacturing variability," Opt. Express **25**(9), 9712–9733 (2017).
3. Y. Xing, J. Dong, S. Dwivedi, U. Khan, and W. Bogaerts, "Accurate extraction of fabricated geometry using optical measurement," Photonics Res. **6**(11), 1008–1020 (2018).
4. Y. Xing, M. Wang, A. Ruocco, J. Geessels, U. Khan, and W. Bogaerts, "Extracting multiple parameters from a compact circuit for performance evaluation," in *European Conference on Integrated Optics, Belgium*, (2019).
5. W. Bogaerts and L. Chrostowski, "Silicon photonics circuit design: methods, tools and challenges," Laser Photonics Rev. **12**(4), 1700237 (2018).
6. S. Dwivedi, H. D'heer, and W. Bogaerts, "Maximizing fabrication and thermal tolerances of all-silicon FIR wavelength filters," IEEE Photonics Technol. Lett. **27**(8), 871–874 (2015).
7. M. Uenuma and T. Motooka, "Temperature-independent silicon waveguide optical filter," Opt. Lett. **34**(5), 599–601 (2009).
8. B. Guha, A. Gondarenko, and M. Lipson, "Minimizing temperature sensitivity of silicon Mach-Zehnder interferometers," Opt. Express **18**(3), 1879–1887 (2010).
9. S. Dwivedi, H. D'heer, and W. Bogaerts, "A compact all-silicon temperature insensitive filter for WDM and bio-sensing applications," IEEE Photonics Technol. Lett. **25**(22), 2167–2170 (2013).
10. P. Xing and J. Viegas, "Broadband CMOS-compatible SOI temperature insensitive Mach-Zehnder interferometer," Opt. Express **23**(19), 24098–24107 (2015).
11. P. Dong, W. Qian, H. Liang, R. Shafiiha, D. Feng, G. Li, J. E. Cunningham, A. V. Krishnamoorthy, and M. Asghari, "Thermally tunable silicon racetrack resonators with ultralow tuning power," Opt. Express **18**(19), 20298–20304 (2010).
12. Y. Yanagase, S. Suzuki, Y. Kokubun, and Sai Tak Chu, "Box-like filter response and expansion of FSR by a vertically triple coupled microring resonator filter," J. Lightwave Technol. **20**(8), 1525–1529 (2002).
13. F. Xia, M. Rooks, L. Sekaric, and Y. Vlasov, "Ultra-compact high order ring resonator filters using submicron silicon photonic wires for on-chip optical interconnects," Opt. Express **15**(19), 11934–11941 (2007).
14. M. S. Dahlem, C. W. Holzwarth, A. Khilo, F. X. Kärtner, H. I. Smith, and E. P. Ippen, "Reconfigurable multi-channel second-order silicon microring-resonator filterbanks for on-chip WDM systems," Opt. Express **19**(1), 306–316 (2011).

Optics EXPRESS

15. S. Feng, T. Lei, H. Chen, H. Cai, X. Luo, and A. W. Poon, "Silicon photonics: from a microresonator perspective," Laser Photonics Rev. **6**(2), 145–177 (2012).
16. J. Lloret, J. Sancho, M. Pu, I. Gasulla, K. Yvind, S. Sales, and J. Capmany, "Tunable complex-valued multi-tap microwave photonic filter based on single silicon-on-insulator microring resonator," Opt. Express **19**(13), 12402–12407 (2011).
17. D. Pérez, I. Gasulla, L. Crudgington, D. J. Thomson, A. Z. Khokhar, K. Li, W. Cao, G. Z. Mashanovich, and J. Capmany, "Multipurpose silicon photonics signal processor core," Nat. Commun. **8**(1), 636 (2017).
18. A. Li, T. Van Vaerenbergh, P. De Heyn, P. Bienstman, and W. Bogaerts, "Backscattering in silicon microring resonators: a quantitative analysis," Laser Photonics Rev. **10**(3), 420–431 (2016).
19. F. G. Peternella, B. Ouyang, R. Horsten, M. Haverdings, P. Kat, and J. Caro, "Interrogation of a ring-resonator ultrasound sensor using a fiber Mach-Zehnder interferometer," Opt. Express **25**(25), 31622–31639 (2017).